Solar Modulation of Cosmic Nuclei over a Solar Cycle: Results from the Alpha Magnetic Spectrometer - SUPPLEMENTAL MATERIAL -

For references see the main text.

Detector.— AMS is a general purpose high energy particle physics detector in space. The layout of the detector is shown in Fig. S1. The key elements are the permanent magnet, the silicon tracker, and four planes of time of flight (TOF) scintillation counters. AMS also contains a transition radiation detector (TRD), a ring imaging Čerenkov detector (RICH), an electromagnetic calorimeter (ECAL), and an array of 16 anticoincidence counters (ACC).

The AMS coordinate system is concentric with the magnet. The x axis is parallel to the main component of the magnetic field and the z axis points vertically with $z = 0$ at the center of the magnet. The (y-z) plane is the bending plane.

The central field of the magnet is 1.4 kG. Before flight, the field was measured in 120 000 locations to an accuracy of better than 2 G.

The tracker has nine layers, the first ($L1$) at the top of the detector, the second ($L2$) above the magnet, six ($L3$ to $L8$) within the bore of the magnet, and the last ($L9$) above the ECAL. $L2$ to $L8$ constitute the inner tracker. Each tracker layer provides an independent measurement of the charge Z. The charge resolution of the combined inner tracker is of $\Delta Z/Z$ = 1–4% for $2 \leq Z \leq 8$ [24]The spatial resolution in each tracker layer is 5–7 µm in the bending direction for $2 \leq Z \leq 8$ events [25]. Together, the tracker and the magnet measure the rigidity R of charged cosmic rays with a maximum detectable rigidity of 3.2–3.7 TV over the 3 m lever arm from $L1$ to $L9$.

The pulse heights of the two TOF upper planes are combined to provide an independent measurement of the charge with an accuracy of $\Delta Z/Z$ = 2–5% for $2 \leq Z \leq 8$ [21]. The pulse heights from the two lower planes are combined to provide another independent charge measurement with the same accuracy.

Nuclei traversing AMS were triggered as described in Ref. [23]. The trigger efficiency has been measured as being $> 81\%$ for He and $> 98\%$ for Li, Be, B, C, N, and O. The Monte Carlo simulation agrees with the measured trigger efficiency within 0.5%.

Monte Carlo simulated events were produced using a dedicated program developed by the collaboration based on the GEANT4-10.1 package [22]. The program simulates electromagnetic and hadronic interactions of particles in the material of the AMS and generates detector responses. The Monte Carlo event samples have sufficient statistics such that they do not contribute to the errors.

Event Selection.— AMS collected 2.12×10^{11} cosmic ray events from May 2011 to November 2022. The collection time used in the light nuclei fluxes analysis includes only those seconds during which the detector was in normal operating conditions and, in addition, AMS was pointing within 30° and the ISS was outside of the South Atlantic Anomaly. Due to the influence of the geomagnetic field, this collection time for galactic cosmic rays increases with rigidity; it is 9.6×10^4 s at 2 GV, 3.3×10^5 s at 5 GV, 7.3×10^5 s at 10 GV, 1.1×10^6 s at 20 GV, reaching 1.6×10^6 s above 30 GV per Bartels rotation on average.

Events are required to be downward going, to have a reconstructed track in the inner tracker, and to pass through $L1$. Track fitting quality criteria, such as a χ^2/d.o.f. < 10 in the bending plane, are applied. Charge measurement selections and quality criteria are applied similar to Ref. [7–9].

The measured rigidity is required to be greater than a factor of 1.2 times the maximum geomagnetic cutoff within the AMS field of view. The cutoff was calculated by backtracing particles from the top of the AMS out to 50 Earth's radii using the most recent International Geomagnetic Reference Field (IGRF) model [26].

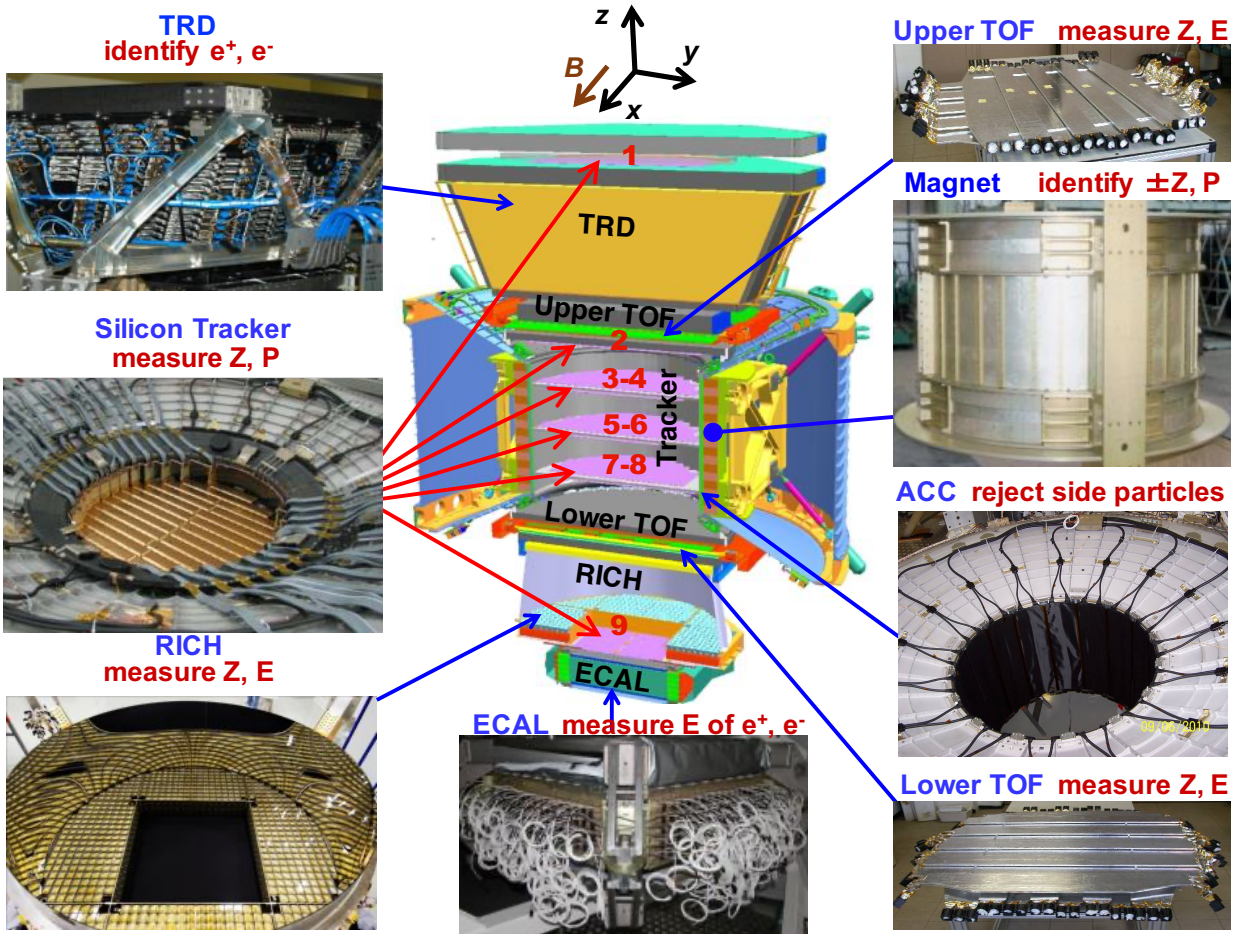

FIG. S1. The AMS detector showing the main elements and their functions. AMS is a TeV precision, multipurpose particle physics magnetic spectrometer in space. It identifies particles and nuclei by their charge Z, energy E, and momentum P or rigidity ($R = P/Z$), which are measured independently by the Tracker, TOF, RICH, and ECAL. The ACC counters, located in the magnet bore, are used to reject particles entering AMS from the side. The AMS coordinate system, concentric with the magnet, is also shown. The x axis is parallel to the main component of the magnetic field and the z axis is pointing vertically.

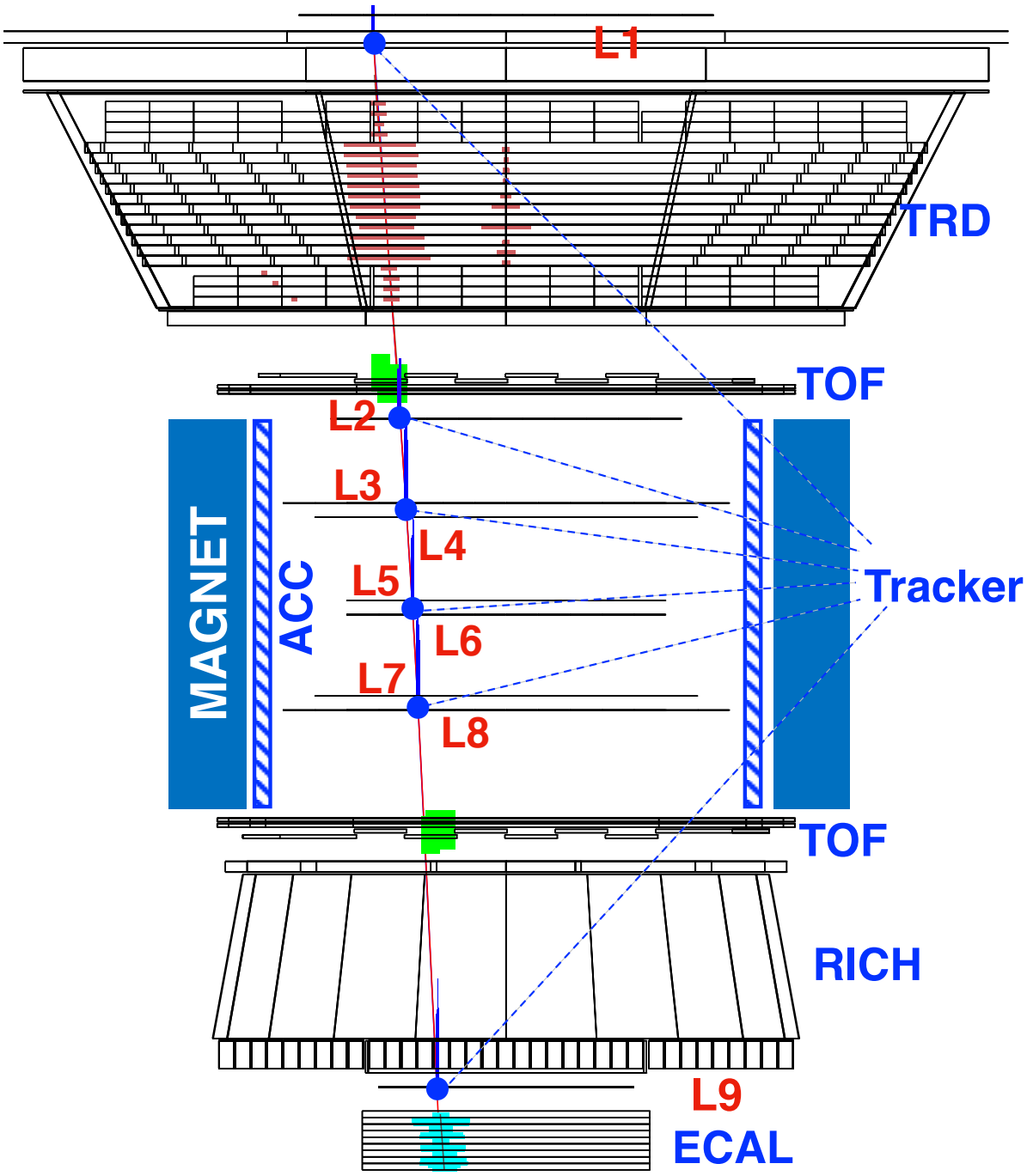

FIG. S2. An event display in the bending plane of a downward-going oxygen nucleus (Z=8) with R = 2.31 GV. The red line indicates the reconstructed trajectory. The magenta spread in TRD shows the dE/dx measurements in different TRD layers, green areas in upper and lower TOF carry the information of the dE/dx as well as the coordinate measurements. The vertical blue lines in the tracker layers carry the information of coordinates and dE/dx or pulse heights. The light blue area in ECAL shows the shower development.

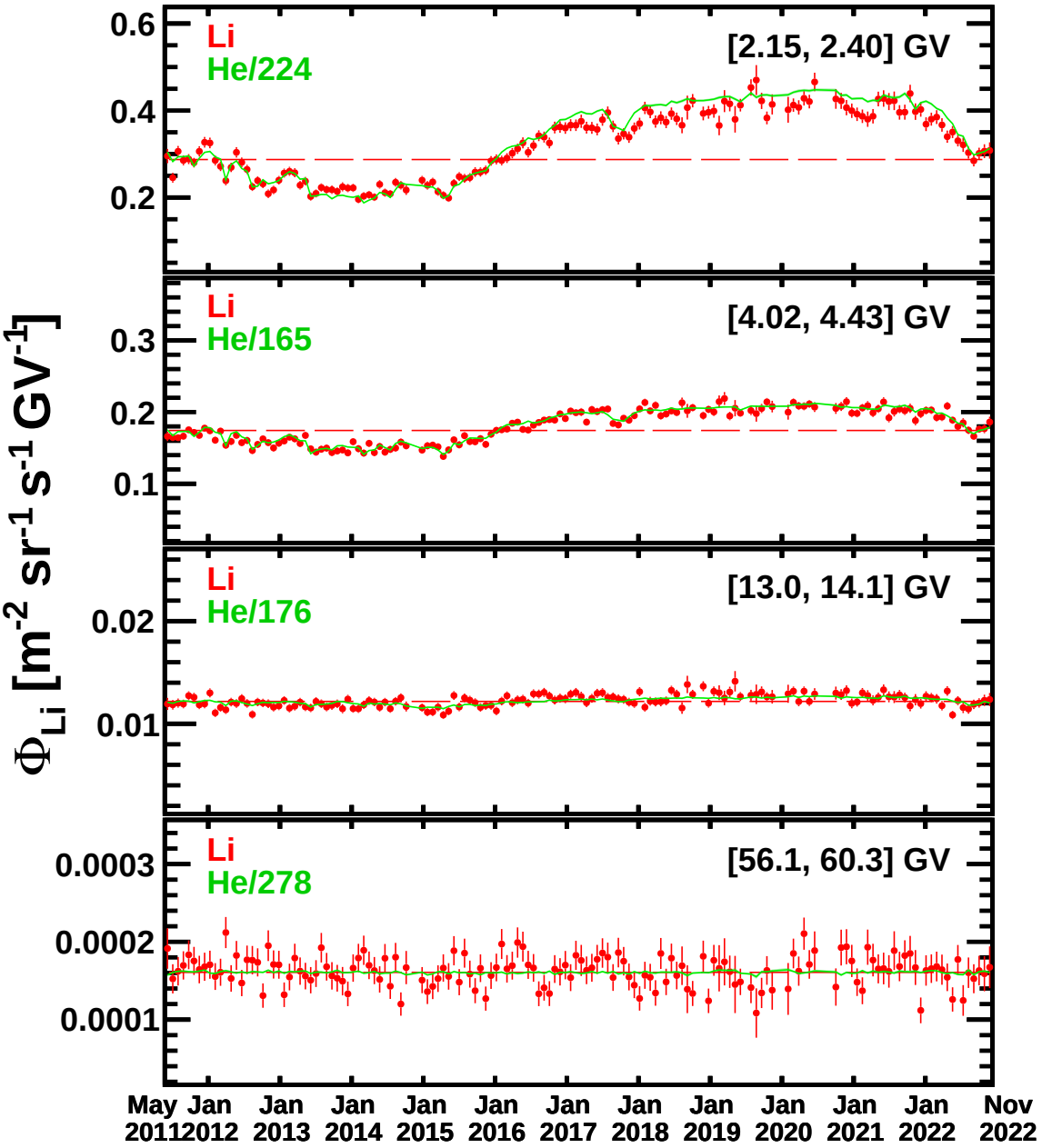

FIG. S3. The AMS Li flux as a function of time for four characteristic rigidity bins. The errors are the quadratic sum of the statistical and time-dependent systematic errors. For comparison, the AMS He flux scaled to match the Li flux average is superimposed as a green curve. As seen, the two fluxes exhibit similar short and long-term structures. The amplitude of the time structures decreases with increasing rigidity. The time-averaged Li flux is shown as a dashed line. In the highest rigidity bin (56.1 to 60.3 GV) the time-averaged Li flux has no observable difference from the time-dependent He flux.

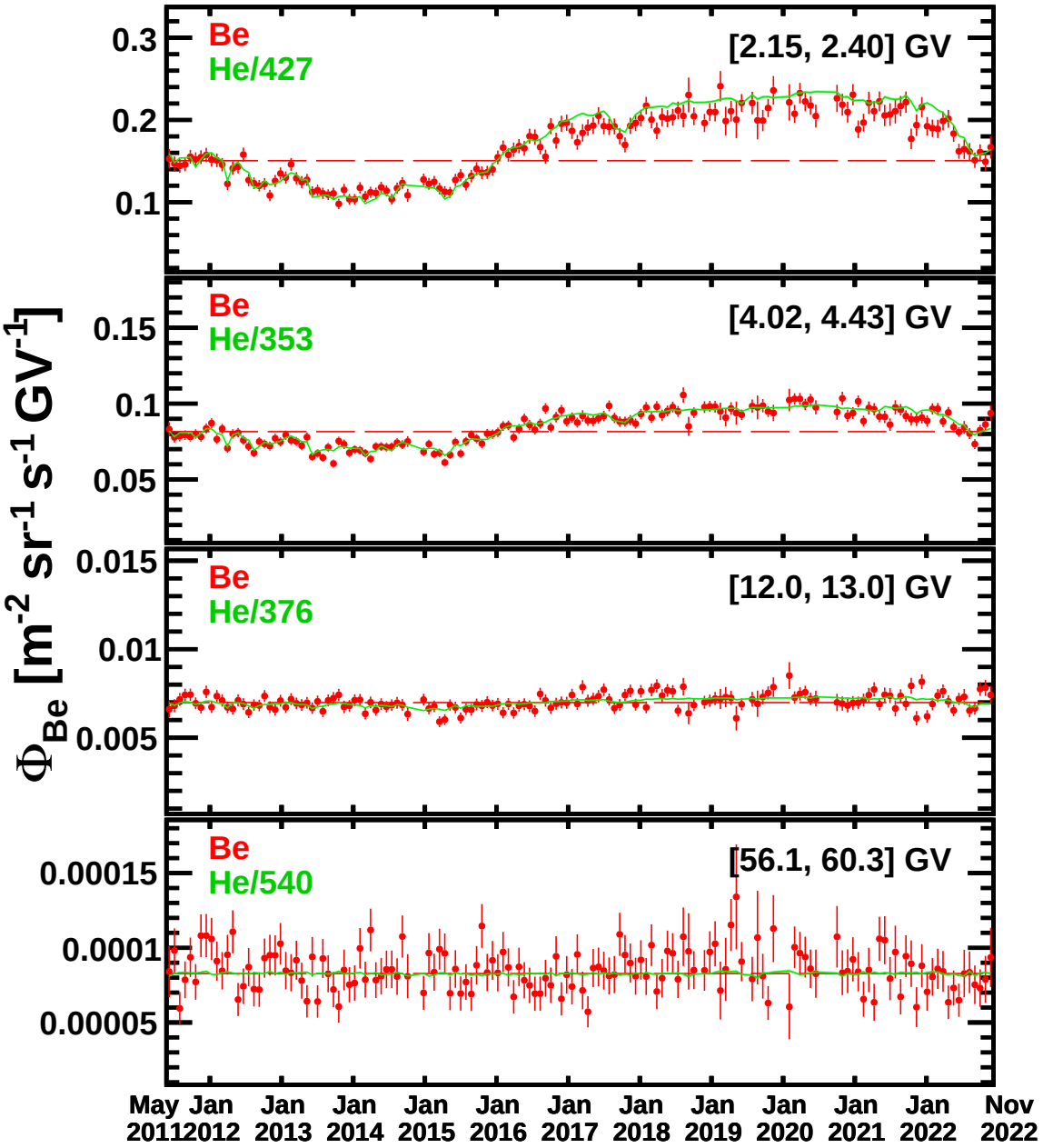

FIG. S4. The AMS Be flux as a function of time for four characteristic rigidity bins. The errors are the quadratic sum of the statistical and time-dependent systematic errors. For comparison, the AMS He flux scaled to match the Be flux average is superimposed as a green curve. As seen, the two fluxes exhibit similar short and long-term structures. The amplitude of the time structures decreases with increasing rigidity. The time-averaged Be flux is shown as a dashed line. In the highest rigidity bin (56.1 to 60.3 GV) the time-averaged Be flux has no observable difference from the time-dependent He flux.

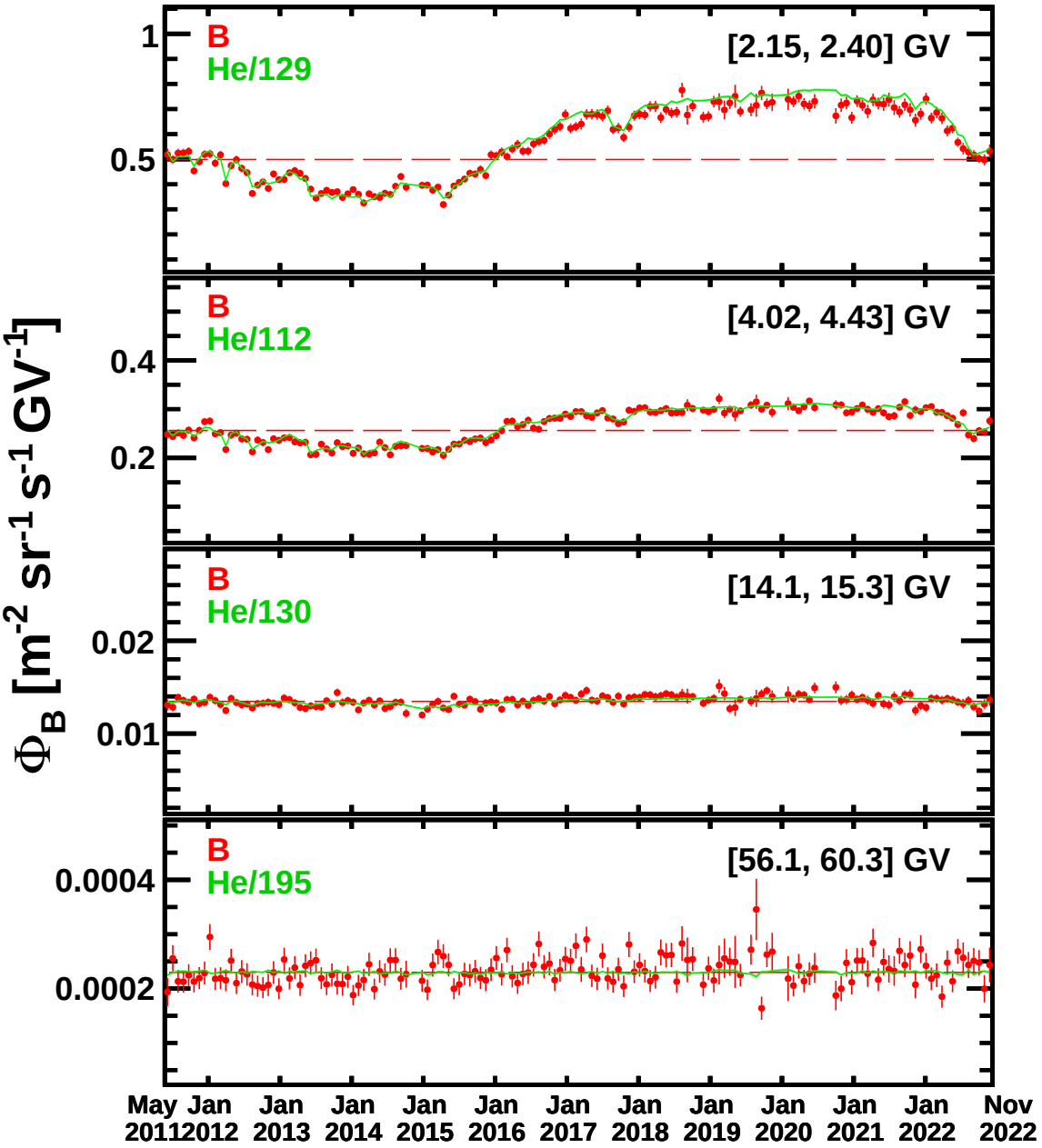

FIG. S5. The AMS B flux as a function of time for four characteristic rigidity bins. The errors are the quadratic sum of the statistical and time-dependent systematic errors. For comparison, the AMS He flux scaled to match the B flux average is superimposed as a green curve. As seen, the two fluxes exhibit similar short and long-term structures. The amplitude of the time structures decreases with increasing rigidity. The time-averaged B flux is shown as a dashed line. In the highest rigidity bin (56.1 to 60.3 GV) the time-averaged B flux has no observable difference from the time-dependent He flux.

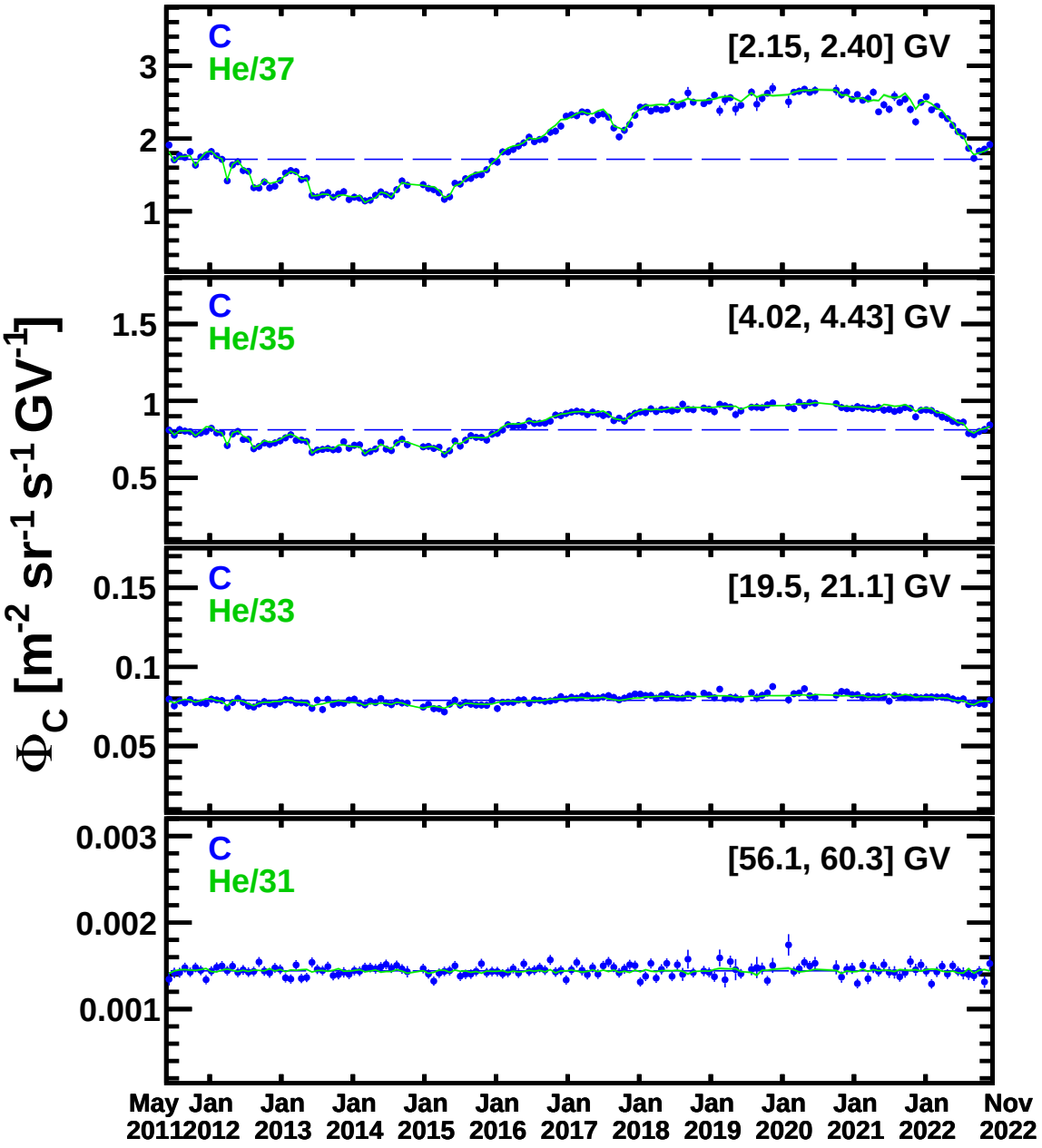

FIG. S6. The AMS C flux as a function of time for four characteristic rigidity bins. The errors are the quadratic sum of the statistical and time-dependent systematic errors. For comparison, the AMS He flux scaled to match the C flux average is superimposed as a green curve. As seen, the two fluxes exhibit similar short and long-term structures. The amplitude of the time structures decreases with increasing rigidity. The time-averaged C flux is shown as a dashed line. In the highest rigidity bin (56.1 to 60.3 GV) the time-averaged C flux has no observable difference from the time-dependent He flux.

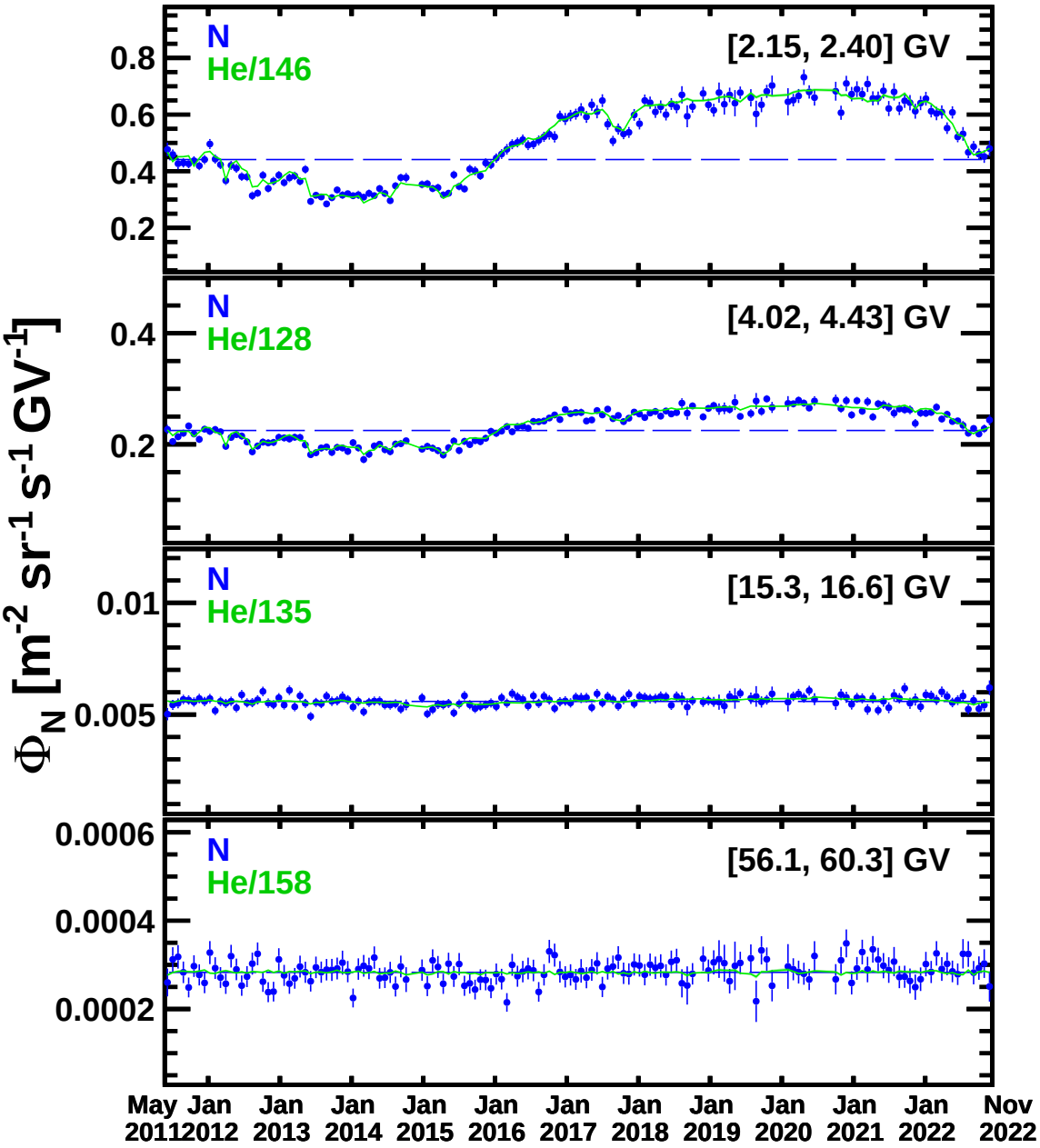

FIG. S7. The AMS N flux as a function of time for four characteristic rigidity bins. The errors are the quadratic sum of the statistical and time-dependent systematic errors. For comparison, the AMS He flux scaled to match the N flux average is superimposed as a green curve. As seen, the two fluxes exhibit similar short and long-term structures. The amplitude of the time structures decreases with increasing rigidity. The time-averaged N flux is shown as a dashed line. In the highest rigidity bin (56.1 to 60.3 GV) the time-averaged N flux has no observable difference from the time-dependent He flux.

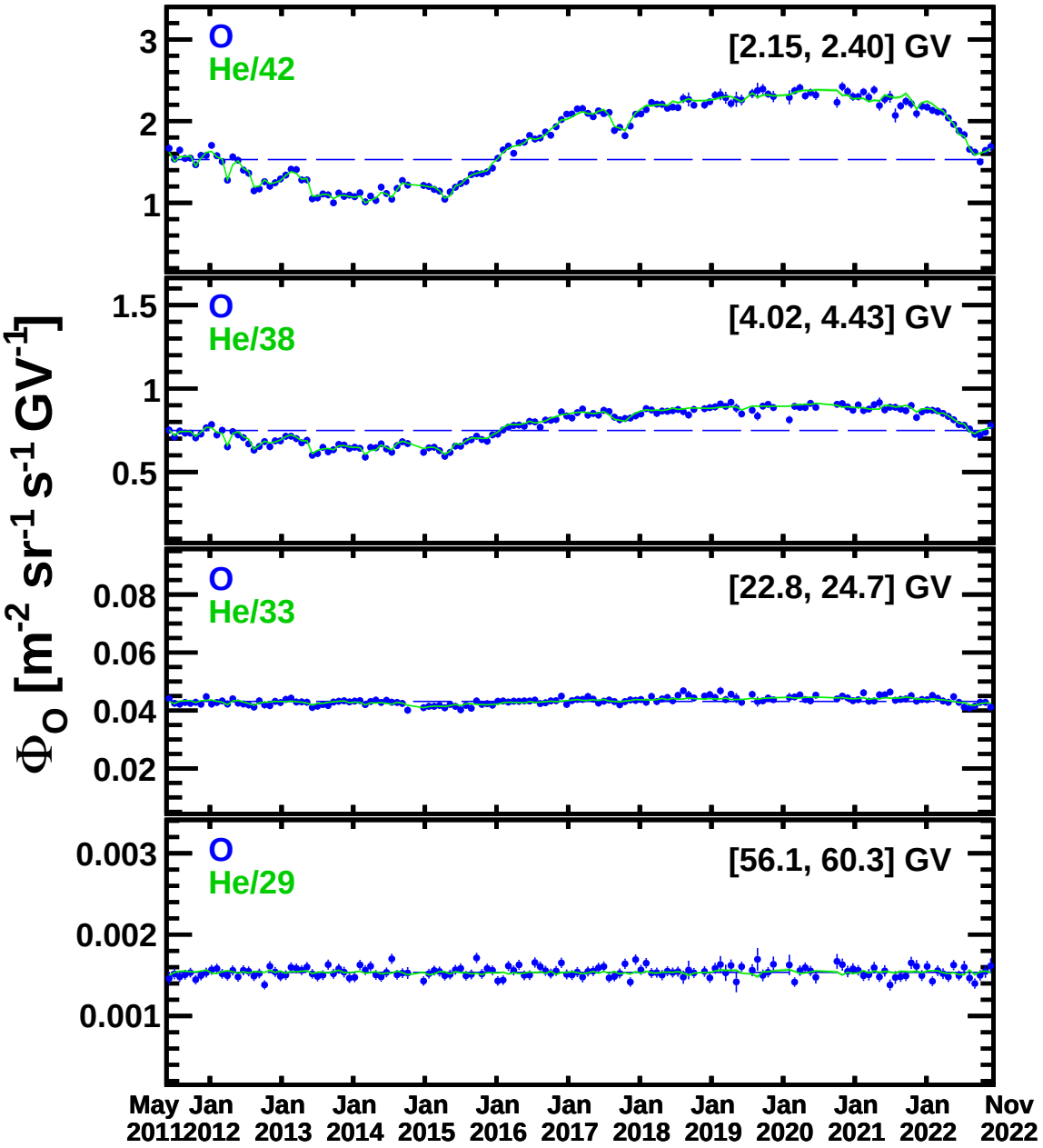

FIG. S8. The AMS O flux as a function of time for four characteristic rigidity bins. The errors are the quadratic sum of the statistical and time-dependent systematic errors. For comparison, the AMS He flux scaled to match the O flux average is superimposed as a green curve. As seen, the two fluxes exhibit similar short and long-term structures. The amplitude of the time structures decreases with increasing rigidity. The time-averaged O flux is shown as a dashed line. In the highest rigidity bin (56.1 to 60.3 GV) the time-averaged O flux has no observable difference from the time-dependent He flux.

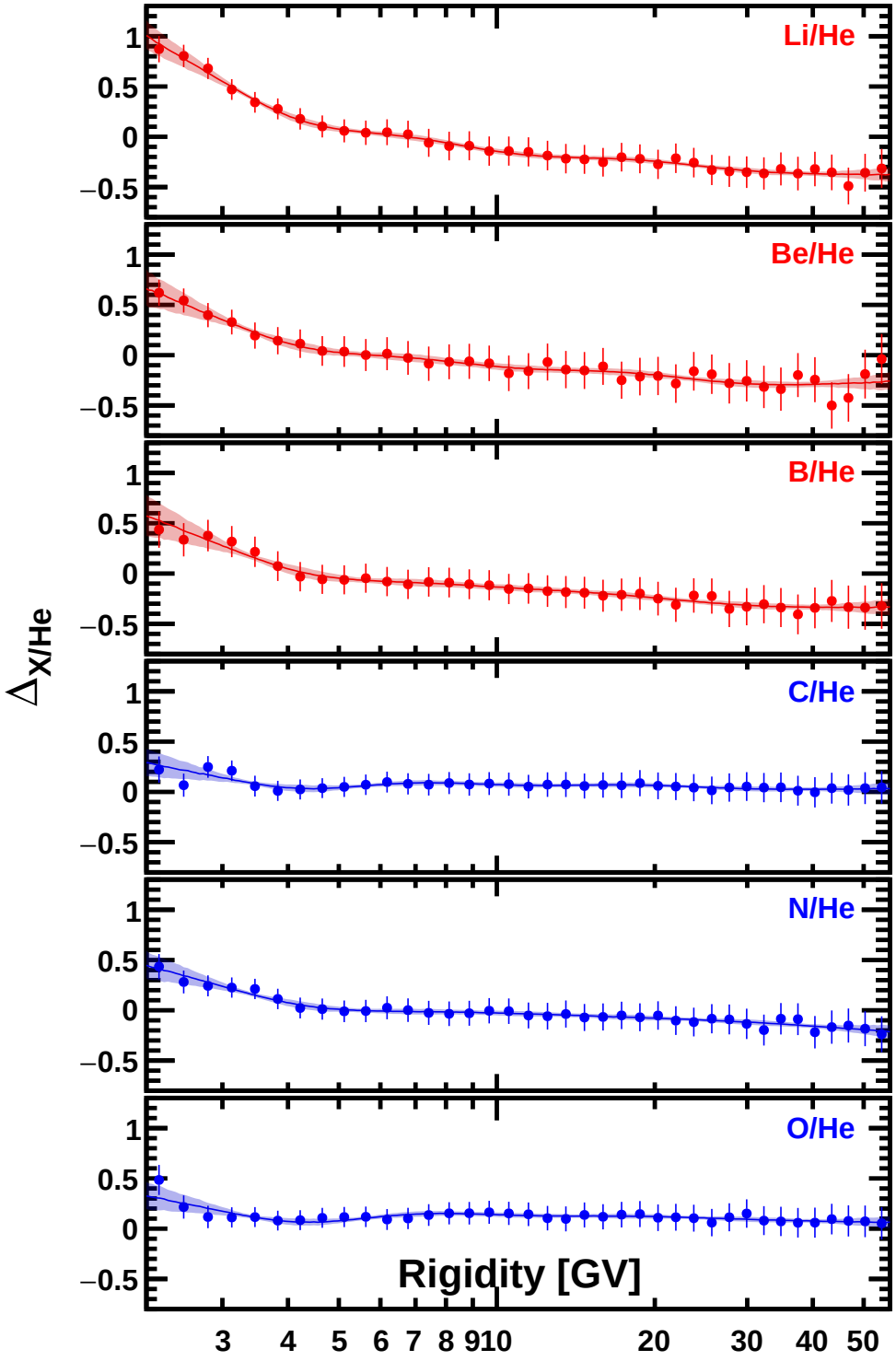

FIG. S9. Spectral indices of the 11.5 years time-averaged flux ratios of Li/He, Be/He, B/He, C/He, N/He, and O/He as a function of rigidity, obtained with fitting the flux ratios with Eq. (3) in moving windows of three bins. The solid curves show the parametrization of the spectral indices using a spline function with knots at 2.7, 3.6, 4.9, 8.5, 14.1, 22.8, and 56.1 GV, and the shaded bands show the parametrization uncertainties (1σ).

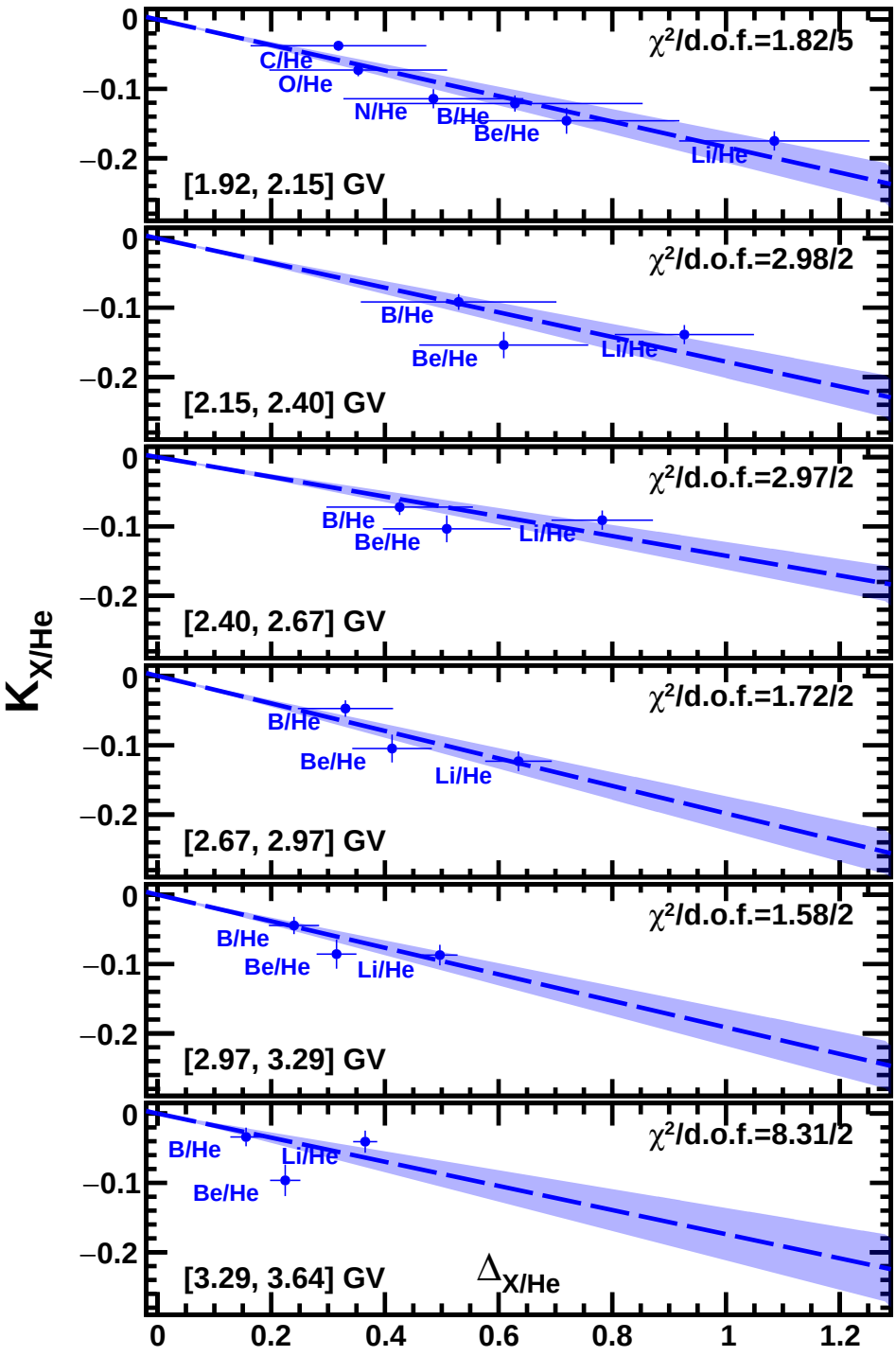

FIG. S10. The dependence of the relative solar modulation magnitude $K_{X/\mathrm{He}}$ on the spectral index $\Delta_{X/\mathrm{He}}$ for the six lowest rigidity bins. From 1.92 GV to 2.15 GV the Li/He, Be/ He, B/He, C/He, N/He, and O/He flux ratios are used. From 2.15 GV to 3.64 GV the Li/He, Be/He, and B/He flux ratios are used. A linear fit with the function $K_{X/\mathrm{He}} = \xi\Delta_{X/\mathrm{He}}$ is also shown as a blue dashed line and 1σ shade. As seen, there is a linear dependence between the relative solar modulation magnitude and the spectral index. Also, the χ^2/d.o.f. is shown in the figure.